Research Paper
Computational Methods for Differential Equations
http://cmde.tabrizu.ac.ir
Vol. 10, No. 4, 2022, pp. 986-1006
DOI:10.22034/cmde.2022.49864.2074

Numerical analysis of fluid flow behaviour in two sided deep lid driven cavity using the finite volume technique

Manoj R. Patel[1,*], **Jigisha U.Pandya**[2], **and Vijay K. Patel**[1]
[1]Department of Mathematics, LDRP Institute of Technology and Research, Kadi Sarva Vishwavidyalaya, Gandhinagar, Gujarat, India.
[2]Department of Mathematics, Sarvajanik College of Engineering and Technology, Surat, Gujarat Technological University, Gujarat, India.

Abstract

In the present study, numerical simulations of two-dimensional steady-state incompressible Newtonian fluid flow in one-sided square and two-sided deep lid driven cavities under the aspect ratio $K = 1, 4, 6$ are reported. For the one-sided lid driven cavity, the upper wall is moved to the right with up to 5000 Reynolds numbers under a grid size of up to 501×501. This lends support to previous findings in the literature with Ghia et al.'s results. Three cases are used in this article for the two-sided deep lid driven square cavity specifically. In these cases, the top and lower walls are moved to the right, while the left and right walls remain fixed up to at high Reynolds numbers (5000) under the grid size of up to 201×201. All possible flow solutions are studied in the present article, and flow bifurcation diagrams are constructed as velocity profiles and streamline contours for the same Reynolds number using a finite volume SIMPLE technique. The work done in this paper includes flow properties such as the location of primary and secondary vortices, velocity components, and numerical values for benchmarking purposes, and it is in excellent agreement with previous findings in the literature. A PARAM Shavak, high-performance computing (HPC) computer, was used to execute the calculations.

Keywords. Partial differential equations, Navier-Stokes equations, Incompressible flow, Lid-driven cavity, Finite volume technique, Boundary value problems.

2010 Mathematics Subject Classification. 65L12, 65M08, 80M12, 80M20,76Rxx.

1. Introduction

Two-dimensional steady state incompressible Newtonian fluid flow in a lid driven square cavity problem has more applications in heat transfer, combustion chambers, mixing vessels, turbine blade tunnels, heat exchangers, aircraft, cars, and massive flow structures of types buildings, cooling towers, and air conditioning systems are some examples in fluid dynamics[1, 23]. Fluid dynamics is an important scientific discipline in which the governing equations are normally differential equations, and analytical solutions are possible for a limited number of cases[19, 22]. For those reasons, numerical methods have been discovered for the estimation of incompressible fluid flow problems[2, 24, 28]. The finite difference techniques, finite-element techniques, and finite-volume techniques are the most common methods for computational fluid dynamics[3, 21].

A Cartesian mesh cannot accurately represent the geometry of most fluid mechanics problems. Instead, the boundaries were generally curved in space. Various engineering problems necessitate incompressible Navier-Stokes simulations of complex fluid flows. The Semi-Implicit Method for Pressure Linked Equations(SIMPLE) algorithm based on finite volume techniques for Navies-stokes equations is the most popular method proposed by Patankar et al [29]. The finite central difference vortices-stream function method is applicable to evaluate the lid driven square cavity problem by Ghia et al[14]. According to Ertuk [9] the lid driven square cavity problem is the most commonly researched field in CFD owing to its comparatively easy computational implementation and intricate behavior, which includes

Received: 11 January 2022 ; Accepted: 01 April 2022.
∗ Corresponding author. Email: manoj_sh@ldrp.ac.in .

counter rotating vortices emerging at the cavity's corners. The backward facing step problem has also been extensively examined, as it illustrates shear-layer detachment and reattachment, which is common to many industrial fluid flow problems, such as airfoils, vehicles, combustors, diffusers, reactor design, and pipe and duct expansions [33]. The finite volume numerical method discretized over a staggered grid has been well analyzed by an iterative solution defined by the SIMPLE algorithm for both cases.[29, 34].

The lid-driven cavity flows problem over the staggered grid has been widely employed. The finite volume method over a staggered grid was used to discover a two-dimensional model to enhance the square cavity driven and controlled by an oscillatory lid [18]. To Solve incompressible fluid flow problems most widely used special kind of technique is finite volume [4, 35]. The method has lots of applications in the field of the heat and fluid flow transfer kind of work [25]. So, To identify the incompressible Newtonian fluid flow numerical solution most suitable method for us is finite volume techniques [7]. Demirdzic et al. [8] used the SIMPLE algorithm to solve inclining the side walls of lid-driven cavity flow. Flux evaluation on the cell boundaries most suitable method is finite-volume techniques[19, 30, 34].

Ghia et al. [14] studied the effectiveness of the coupled strongly implicit multigrid (CSI-MG) method in the determination of high Reynolds number fine-mesh flow solutions using the vorticity-stream function formulation of the two-dimensional incompressible Navier-Stokes equations. The cavity issue was utilized as the foundation for testing the effectiveness of the coupled strongly implicit multi-grid approach for high Reynolds number fine-mesh cavity flow in high Reynolds number fine-mesh cavities. In a research, they looked at Reynolds numbers ranging from 100 to 10000 and uniform mesh sizes of 129×129 for $Re \leq 3200$ and 257×257 for $5000 \leq Re \leq 10,000$, as well as Reynolds numbers ranging from 100 to 10000. The findings clearly show the main vortex, as well as the secondary vortices in both the bottom corners and, for $Re \geq 3200$, also in the top left corners of the diagram.

Erturk et.al.[10](2005) explored the numerical solution of the two-dimensional steady state incompressible Lid-driven cavity flow. The Navier-Stokes equations in stream function-vorticity formulation were calculated numerically using a uniform grid size of 601×601 for $Re \leq 21,000$ with governing equations absolute residuals were less than 10^{-10}. Erturk et. al.[11](2006) studied the new fourth-order compact formulation and the uniqueness of the formulation is the final form of the High-order compact (HOC) formulations. The formulation in the same form as the Navier Stokes equations could be easily applied to the fourth order compact formulation. Erturk et. al. [12](2007) found the numerical solutions of two-dimensional steady state incompressible flow inside a triangular cavity. Using a very fine grid mesh, the triangular cavity flow is solved for higher Reynolds numbers and also the study of triangular cavities for various corner angles was performed.

There have also been some encouraging developments with rectangular cavities. Many industrial applications face cavities of differing depths and not squares, thus researchers have explored the concept of cavity aspect ratios. In 2006, Patil et al. [27] used the Lattice Boltzmann equation (LBE), and conducted simulations using the LBGK model for flow conditions from 50 to 3200 with varying aspect ratios ranging from $K = 1$ to $K = 4$, and changed different Reynolds number ranges, from 50 to 3200. According to their results, Taneda and Chen's conclusions were correct. In the case of cavity flow with Reynolds numbers higher than 3200 and aspect ratios greater than 1, very few studies have been conducted. In a two-dimensional nine-directional lattice model utilizing the lattice Boltzmann technique, Arun et al. [5]conducted research on flow behavior in a two-sided lid-driven cavity on a two-dimensional nine-directional lattice model for various Reynolds numbers (100, 1000, 2000, and 5000) and aspect ratios (1, 2 and 4).

The consequence is that we can see that a significant amount of research has been done on this topic. Researchers like Ghia et al. [14] and Erturk et al. [11] have discovered some of the most promising results for Reynolds numbers up to 21000. Many authors use these results as a benchmark for their work. A number of methods, including the stream function-vorticity, the primitive variable technique, and the Lattice Boltzmann approach, are often used. Only a few scholars have studied the deep cavity region with two walls moving in the same and opposing directions. However, no study in the literature investigated the issue of a cavity driven by a two-sided deep lid-driven for high Reynolds numbers (5000). Specifically, three cases are used to drive the two sided deep lid-driven cavity flow in this article. In these three cases, the top and lower walls are moved to the right, while the left and right walls are kept stationary. Numerical simulations were carried out for the one-sided problem with a Reynolds number of up to 5000 and a mesh size of up to 501, and for the two sided deep lid-driven cavity problem under the aspect ratios of $K = 1, 4, 6$ with a Reynolds number of up to 5000 and a mesh size of up to 201. The occurrence of the vortices profile is investigated.

Additionally, streamlined contour diagrams for the same Reynolds number are created using a finite volume SIMPLE technique.

The finite volume technique is used to study the steady state incompressible fluid flow lid-driven cavity problem. We have introduced the finite volume SIMPLE algorithm to two-dimensional steady state lid cavity flow implemented to our problem in section 2. In section 3, the numerical discretization scheme is derived on a staggered grid by applying the finite volume numerical technique. In section 4, lid-driven one-sided cavity flow numerical results are validated with the standard benchmark solution by Ghia et al and this section contains the Finite volume SIMPLE algorithm validated code. In section 5, two-sided deep lid-driven cavity problems have been analyzed for unmarked case results and contour plots for aspect ratio(AR) $K = 1,\ 4,\ \&\ 6$. Finally, concluding remarks are provided in section 6.

2. Numerical Procedure and Mathematical Modeling

2.1. **Problem description.** Let us take a steady-state viscous two-dimensional incompressible Newtonian internal fluid flow with the size of (1×1). The upper sidewall is moving with $u = 1$ velocity [9, 14] and at the stationary wall, no slip boundary condition applies as per Figure 1. Inside the two-dimensional square cavity, fluid flow is laminar. This movement produced a flow identified close to the smaller secondary vortices and the cavity centre by a larger primary vortex. The cavity, viz, Left Secondary Vortex (Left-SV), Right Secondary Vortex (Right-SV), and Left Upper Secondary Vortex (Left-USV) at the corners are based on the Reynolds number (Re).

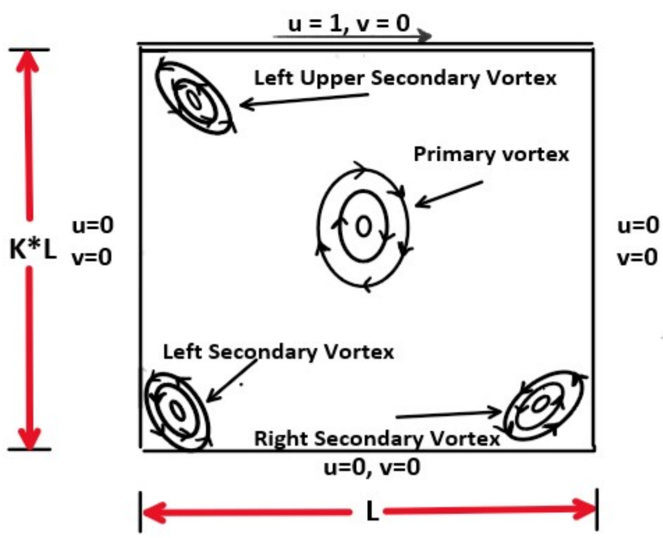

Figure 1. 2D lid driven square cavity One sided flow vortices layout and boundary conditions

2.2. **Governing Equation.** Let us take a steady state viscous two dimension incompressible lid driven square cavity Newtonian internal fluid flow. The incompressible two dimension Navier Stokes equations include the continuity Eq. (2.1), x-momentum Eq. (2.2) and y-momentum Eq. (2.3). The steady state flow of incompressible fluids for continuity and momentum equations in Cartesian coordinates is as follows [6, 13, 31].

$$\frac{\partial(\rho u)}{\partial x} + \frac{\partial(\rho v)}{\partial y} \quad = \quad 0, \tag{2.1}$$

$$\frac{\partial(\rho u \cdot u)}{\partial x} + \frac{\partial(\rho u \cdot v)}{\partial y} \quad = \quad \frac{\partial}{\partial x}\left(\mu \frac{\partial u}{\partial x}\right) + \frac{\partial}{\partial y}\left(\mu \frac{\partial u}{\partial y}\right) - \frac{\partial p}{\partial x}, \tag{2.2}$$

$$\frac{\partial(\rho u \cdot v)}{\partial x} + \frac{\partial(\rho v \cdot v)}{\partial y} = \frac{\partial}{\partial x}\left(\mu \frac{\partial v}{\partial x}\right) + \frac{\partial}{\partial y}\left(\mu \frac{\partial v}{\partial y}\right) - \frac{\partial p}{\partial y}, \tag{2.3}$$

p, ρ, μ, u, and v are pressure, density, dynamic viscosity, velocity components along (x and y) axes, respectively. Solving governing equation by applying finite volume SIMPLE algorithm.

2.3. **Finite volume SIMPLE algorithm.** To evaluate pressure for incompressible flow, we have to solve Eq. (2.1) to (2.3). We observe that Eqs. (2.2) and (2.3) contain non-linear term quantizes that must be solved iteratively from a guessed initial velocity field [29, 36]. Second, the unknown pressure field must be solved iteratively [32, 34]. However, the continuity Eq. (2.1) does not have the pressure as a source term but it's included in Eqs. (2.2) and (2.3). To evaluate this lid-driven square cavity flow problem over a staggered meshing approach to velocity components where the pressure is evaluated at the centre of the control volume (at the node) whereas velocity is calculated at the faces of the control volume. [26, 29, 34]. The grid arrangement for two-dimensional incompressible flow is determined using a staggered grid which is in Figure (2). The linear and non-linear terms of pressure and velocity, respectively in

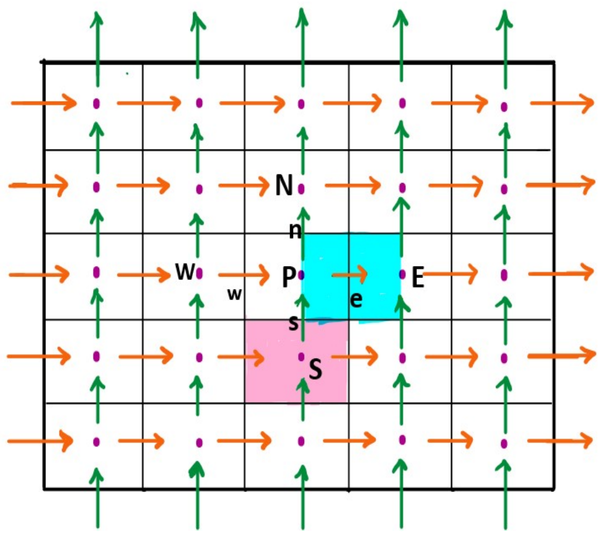

FIGURE 2. Staggered grid discretized

Eqs. (2.2) and (2.3) are evaluated using iteratively. For that, Eqs. (2.1) - (2.3) are first discretized using a finite volume scheme as follow. For discretized Eqs. (2.2) and (2.3) by taking the integration about the control volume described in Figure (2). Now, Solving x-momentum and y-momentum equations.

$$\int_s^n \int_w^e \left[\frac{\partial(\rho u \cdot u)}{\partial x} + \frac{\partial(\rho u \cdot v)}{\partial y}\right] dxdy = \int_s^n \int_w^e \left[-\frac{\partial p}{\partial x}\right] dxdy \quad + \quad \int_s^n \int_w^e \left[\frac{\partial}{\partial x}\left(\mu \frac{\partial u}{\partial x}\right)\right] dxdy + \int_s^n \int_w^e \frac{\partial}{\partial y}\left(\mu \frac{\partial u}{\partial y}\right) dxdy,$$

$$[((\rho u \cdot u)_e \Delta y - (\rho u \cdot u)_w \Delta y)] + [((\rho u \cdot u)_n \Delta x - (\rho u \cdot u)_s \Delta x)] = -\frac{\partial p}{\partial x}\Delta x \Delta y + \left[\mu_e \left(\frac{\partial u}{\partial x}\right)_e \Delta y - \mu_w \left(\frac{\partial u}{\partial x}\right)_w \Delta y\right] + \left[\mu_n \left(\frac{\partial u}{\partial x}\right)_n \Delta x - \mu_s \left(\frac{\partial u}{\partial x}\right)_s \Delta x\right] \tag{2.4}$$

Now, Evaluating diffusion term by using central difference and convective term & pressure term evaluate at $\rho_e = \rho_w = \rho_n = \rho_s = \rho$, $\mu_e = \mu_w = \mu_n = \mu_s = \mu$ and $\Delta x = \Delta y$.

Convective term[26, 29, 34]:

$$[((\rho u \cdot u)_e \Delta y - (\rho u \cdot u)_w \Delta y)] \quad + [((\rho u \cdot u)_n \Delta x - (\rho u \cdot u)_s)\,\Delta x] = \frac{\rho}{2}\Delta y\, u_E\,(u_E + u_P)$$
$$-\frac{\rho}{2}\,\Delta y\, u_W\,(u_P + u_W) + \frac{\rho}{2}\,\Delta x\, u_N\,(u_N + u_P) - \frac{\rho}{2}\,\Delta x\, u_S\,(u_P + u_S). \quad (2.5)$$

Diffusion term[29, 34]:

$$\left[\mu_e \left(\frac{\partial u}{\partial x}\right)_e - \mu_w \left(\frac{\partial u}{\partial x}\right)_w\right] \Delta y \quad = \quad \mu(u_E + u_W), \quad (2.6)$$
$$\text{and} \quad \left[\mu_n \left(\frac{\partial u}{\partial x}\right)_n - \mu_s \left(\frac{\partial u}{\partial x}\right)_s\right] \Delta x \quad = \quad \mu(u_N + u_S). \quad (2.7)$$

Pressure term[29, 34]

$$-\frac{\partial p}{\partial x}\Delta x \Delta y \quad = \quad (p_P - p_E)\,\Delta y. \quad (2.8)$$

Put the value of Eqs. (2.5), (2.6), (2.7), and (2.8) in Eq. (2.4) then we get discretized form of velocity profile in Eq. (2.9)

$$a_{e,u} u_e \quad = \quad a_e u_E + a_w u_W + a_n u_N + a_s u_S + (p_P - p_E)\Delta y, \quad (2.9)$$

where

$$a_{e,u} = a_e + a_w + a_n + a_s,$$
where
$$a_e = -\frac{u_E \Delta y}{2} + \frac{1}{Re}, \quad a_w = \frac{u_W \Delta y}{2} + \frac{1}{Re},$$
$$a_n = -\frac{v_n \Delta x}{2} + \frac{1}{Re}, \quad a_s = \frac{v_S \Delta x}{2} + \frac{1}{Re},$$
$$\text{and} \quad Re = \frac{\rho}{\mu} = \text{ Reynolds number}$$

In a similar manner, The $y-$ momentum equation velocity discretization form in Eq. (2.10)

$$a_{e,v} v_n \quad = \quad A_e v_E + A_w v_W + A_n v_N + A_s v_S + (p_P - p_N)\Delta x, \quad (2.10)$$

where

$$a_{e,v} = A_e + A_w + A_n + A_s,$$
where
$$A_e = -\frac{u_E \Delta x}{2} + \frac{1}{Re}, \quad A_w = \frac{u_W \Delta x}{2} + \frac{1}{Re},$$
$$A_n = -\frac{v_N \Delta y}{2} + \frac{1}{Re}, \quad A_s = \frac{v_S \Delta y}{2} + \frac{1}{Re},$$
$$\text{and} \quad Re = \frac{\rho}{\mu} = \text{ Reynolds number}$$

The x-momentum Eq. (2.9) in terms of the general discretized form of neighbouring nodes as in Eq. (2.12)

$$a_{e,u} u_e \quad = \quad \sum a_{nb,u} u_{nb,u} + b + (p_P \Delta y - p_E \Delta y), \quad (2.11)$$
$$u_e \quad = \quad \frac{\sum a_{nb,u} u_{nb,u} + b}{a_{e,u}} + d_e(p_P - p_E), \quad (2.12)$$

where b is source term that arising from pressure gradient and $d_e = \frac{\Delta y}{a_{e,u}}$.
In a similar manner, The $y-$ momentum equation as in Eq. (2.14)

$$a_{n,v} v_n = \sum a_{nb,v} v_{nb,v} + b + (p_P \Delta x - p_E \Delta x), \tag{2.13}$$

$$v_n = \frac{\sum a_{nb,v} v_{nb,v} + b}{a_{n,v}} + d_n(p_P - p_N) \tag{2.14}$$

where b is source term that arising from pressure gradient and $d_n = \frac{\Delta x}{a_{n,v}}$
let us guess pressure p as p^*, the approximate velocity u^* and v^* which written as in Eq. (2.15) and (2.16)

$$a_{e,u} u_e^* = \sum a_{nb,u} u_{nb,u}^* + b + (p_P^* \Delta y - p_E^* \Delta y) \text{ and} \tag{2.15}$$

$$a_{n,v} v_n^* = \sum a_{nb,v} v_{nb,v}^* + b + (p_P^* \Delta x - p_N^* \Delta x) \tag{2.16}$$

subtract Eqs. (2.11) and (2.15) , Eqs. (2.13) and (2.16) we get

$$a_{e,u} u_e' = \sum a_{nb,u} u_{nb,u}' + (p_P' \Delta y - p_E' \Delta y) \text{ and} \tag{2.17}$$

$$a_{n,v} v_n' = \sum a_{nb,v} v_{nb,v}' + (p_P' \Delta x - p_N' \Delta x) \tag{2.18}$$

where $u_e = (u_e^* + u_e')$, $v_n = v_n^* = v_n'$, $p = p^* + p'$ and u' and v' are correction velocity.
For the SIMPLE algorithm [29, 34] the summation term in Eqs. (2.17) and (2.18) are omitted. Consequently, the velocity correction can be written as in Eq. (2.19)

$$u_e' = (d_e p_P' - d_e p_E'), \qquad v_n' = (d_n p_P' - d_n p_N') \tag{2.19}$$

Now, the Continuity Eq. (2.1) is discretized over the main control volume and then evaluated pressure correction p'.

$$\int_s^n \int_w^e \left[\frac{\partial(\rho u)}{\partial x} + \frac{\partial(\rho u)}{\partial y} \right] dx dy = ((\rho u)_e \Delta y - (\rho u)_w \Delta y) + ((\rho v)_n \Delta x - (\rho v)_s \Delta x) \tag{2.20}$$

Putting the value of $u_e = u_e^* + (d_e p_P' - d_e p_E')$, $u_w = u_w^* + (d_w p_W' - d_w p_P')$, $v_n = v_n^* + (d_n p_P' - d_n p_N')$ and $v_s = u_s^* + (d_s p_S' - d_s p_P')$ in Eq. (2.20), then we get pressure correction discretization form in Eq. (2.21) at $\rho_e = \rho_w = \rho_n = \rho_s = \rho$

$$a_P \cdot p_P' = a_E \cdot p_E' + a_W \cdot p_W' + a_N \cdot p_N' + a_S \cdot p_S' + q \tag{2.21}$$

where

$$a_E = \rho \cdot d_e \Delta y, \quad a_W = \rho \cdot d_w \Delta y, \quad a_N = \rho \cdot d_n \Delta x, \quad a_S = \rho \cdot d_s \Delta x,$$
$$q = \rho \cdot (u_w^* \Delta y - u_e^* \Delta y) + \rho \cdot (u_s^* - u_n^*),$$
$$a_P = a_E + a_W + a_N + a_S$$

In Eqs. (2.17) and (2.18) omitting summation terms. So for simplification, we required some relaxation operator α_p such that pressure become as $p = p^* + \alpha_p p'$, for the optimal solution relaxation factor α_p are dependent [29, 34]. For the instance suggest $\alpha_p = 0.5$ and $\alpha_p = 0.8$ for the li driven cavity problem [34].

3. Numerical results and discussion

The square cavity lid driven problem is simulated by using MATLAB for 100, 400, 1000, 2000 and 5000 Reynolds numbers with size of grids 51, 101, 201 and 501. The numerical results of these simulations are validated using the square lid driven cavity midpoint $u-$velocity as correlated with the results of Ghia et al (1982)[14], as shown in the Figure 3 – 5.

The Square lid-driven one-sided cavity for the streamlines contour is shown in Figure 3 for different Re 400, 1000, 2000, and 5000 with gride sizes of 501. Intensive streamlines indicate that the Primary Vortex (PV) takes place close to the cavity centre and it depends on the secondary eddies which take place at the corners, as given in Figure 3. The Right-SV and Left-SV occur at Re numbers 100 & 400 and Right-SV, Left-SV, Left-USV occurs at Re numbers 2000

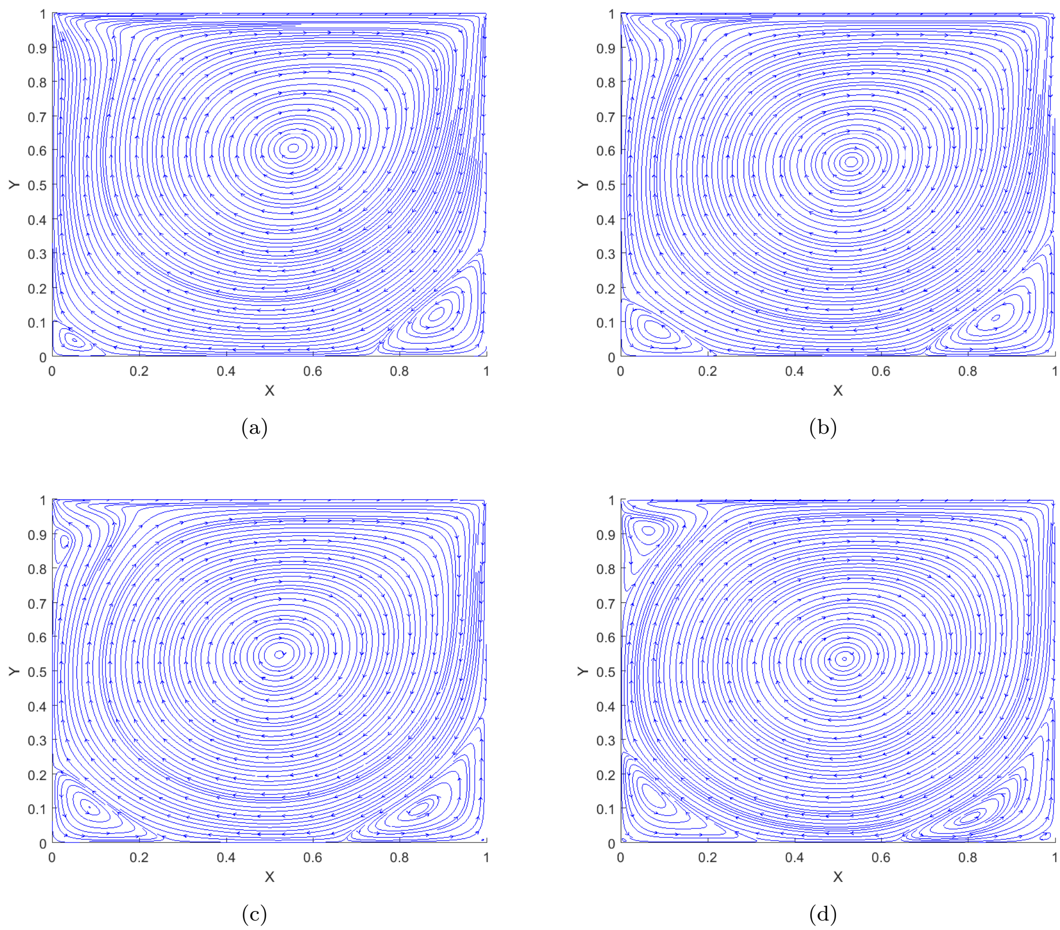

FIGURE 3. Streamlines contour of square one-side lid driven cavity (a) Re.No.=400, (b) Re.No.=1000, (c) Re.No.=2000, (d)Re.No.=5000, Grid 501 × 501

& 5000. The largest size of Secondary Vortex (SV) & Primary Vortex (PV) converges at the cavity centre when the Reynolds numbers are higher as shown in Figure 3.

One sides square lid cavity, Figure 3 shows the midplane u-velocities for different Reynolds numbers. The maximum velocity in the top wall is represented as 1 in the graph, which moves in the right side direction. When Re increases, there is a linear change in the velocity profile in the middle of the cavity. Figure 4 shows the midplane v-velocities for different Reynolds numbers. The data is compared with the present study for velocity profile with velocity profile given by Ghia. et al[14] for 100, 400, 1000, and 5000 Re and the velocity profile given by Hou. et al[17] for 2000 Re as shown in Figures 3 and 4. The present results demonstrate that they are perfectly correlated with the data. The velocity contour of the lid is driven by one side square cavity for the Reynolds No. 2000 and 5000 on gride 501 shows in the Figure 5.

Table 1 shows the performance of a convergence analysis to determine the convergence speed that is related to the computed speed and number of iterations. However, the computations have been conducted on PARAM Shavak high-performance computing (HPC) computer, Intel Xeon with RAM-96GB with 2400-MHz using programming in MATLAB software[15]. From Table 1, it is concluded that a numerical technique takes CPU time and iterations with the increase of both the mesh size and Reynolds numbers until it reaches the convergence criteria.

Table 1. Grid Size with No. of iterations and time for convergence

Renols number (Re)	Gride size	Convergence Iterations (error = 10^{-7})	Time(s)
100	51*51	3735	10.5264
	101*101	12111	25.8530
	201*201	36362	342.6613
	501*501	144838	7616.4443
400	51*51	3846	10.7546
	101*101	12293	26.4664
	201*201	52637	239.1340
	501*501	229908	12554.4187
1000	51*51	15355	14.0277
	101*101	45396	72.0553
	201*201	138106	910.2772
	501*501	574144	30454.8571
2000	51*51	124145	53.8760
	101*101	381595	566.3873
	201*201	1155499	7555.7716
	501*501	4335278	273756.4652
5000	51*51	176055	72.6275
	101*101	551336	796.1188
	201*201	1590514	10902.9264
	501*501	6808631	402215.0943

Table 2. lid driven One sided square cavity with present study for Re. No. 100,400 and 1000

Re. No.	Vortex position		Present	Ghia et al	Hou et a	Gupta et al	Kamel et al
100	PV	x	0.6171	0.6171	0.6196	0.6125	0.6132
		y	0.722	0.7344	0.7372	0.7375	0.7400
	Right-SV	x	0.9453	0.9453	0.9451	0.9375	0.9400
		y	0.06193	0.0625	0.0627	0.0625	0.06000
	Left-SV	x	0.03146	0.0313	0.0391	0.0374	0.0333
		y	0.03853	0.0391	0.0352	0.0374	0.03330
400	PV	x	0.5547	0.5546	0.5607	0.5500	0.5550
		y	0.5937	0.6055	0.6078	0.6125	0.6049
	Right-SV	x	0.89059	0.89059	0.8901	0.8874	0.8850
		y	0.1195	0.125	0.1255	0.125	0.12
	Left-SV	x	0.0508	0.0507	0.0548	0.0500	0.0500
		y	0.0471	0.0468	0.0509	0.0500	0.0500
1000	PV	x	0.5311	0.5312	0.5333	0.5250	0.5300
		y	0.55059	0.5625	0.5646	0.5625	0.5649
	Right-SV	x	0.8592	0.8594	0.8667	0.8625	0.8649
		y	0.115	0.1094	0.1137	0.1125	0.115
	Left-SV	x	0.08584	0.0859	0.0902	0.0874	0.0850
		y	0.07674	0.0781	0.0783	0.074	0.0749

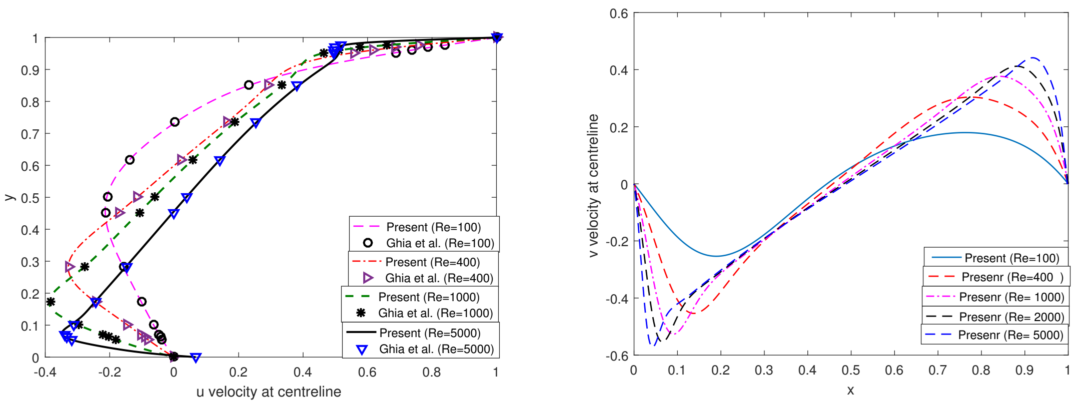

(a) (b)

FIGURE 4. (a) lid driven One sided square cavity flow of centerline velocity u., (b)lid driven One sided square cavity flow of centerline velocity v.

TABLE 3. One-sided square lid-driven cavity verification with present study for Re (2000 and 5000)

Reynolds number	Vortex position		Present	Hou et al	Gupta et al	Kamel et al
2000	PV	x	0.5251	0.5254	0.5250	0.5250
		y	0.5583	0.5490	0.5500	0.5500
	Right-SV	x	0.8450	0.8470	0.8375	0.8449
		y	0.08475	0.09800	0.1	0.1
	Left-SV	x	0.08498	0.0902	0.0874	0.0850
		y	0.1034	0.1058	0.1000	0.1050
	Left-USV	x	0.0300	-	0.0374	0.03
		y	0.8595	-	0.8874	0.8800
5000	PV	x	0.5144	0.5175	0.5124	-
		y	0.5386	0.5373	0.5374	-
	Right-SV	x	0.8001	0.8077	0.8000	-
		y	0.0866	0.0744	0.074	-
	Left-SV	x	0.0757	0.0783	0.074	-
		y	0.1382	0.1373	0.1313	-
	Left-USV	x	0.06883	0.06669	0.0688	-
		y	0.8967	0.9098	0.9124	-

The results obtained in Tables 1, 2, and 3 show that this current finite-volume computational technique has a better agreement with the results obtained by Ghia. et. al. [14], Hou. et. al. [17], Gupta. et. al. [16], and Kamel. et. al. [20] using different numerical techniques. The finite volume simple algorithm numerical technique code verification of one-sided lid-driven cavity work and the deep lid-driven two-sided cavity concludes in section 4.

4. Two sided lid driven deep cavity flow

The geometry of the present problem is shown in Figure 6. It consists of a two-dimensional two-sided deep lid-driven cavity with the height $K \times L$ and the width L. In this two-sided deep lid-driven cavity both walls, upper and lower, move to the right, whereas right and left walls lept as stationary. For the present work, aspect ratio (AR) is

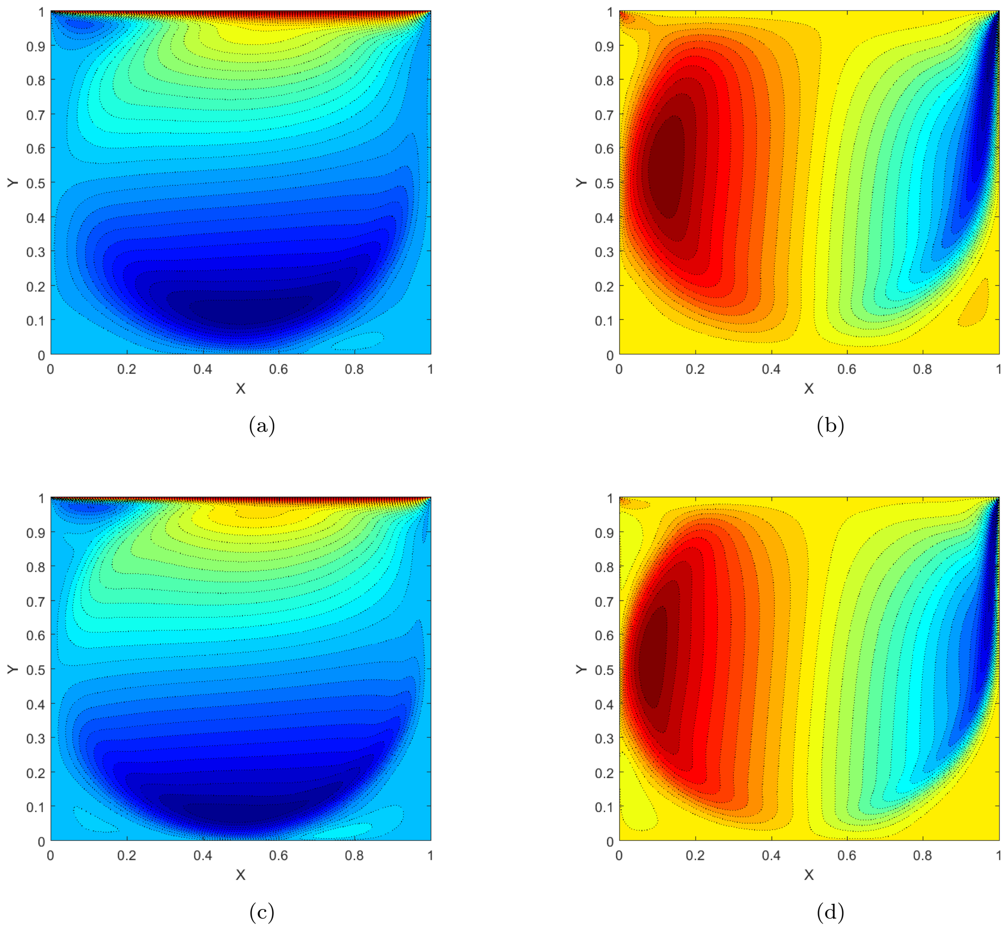

FIGURE 5. Velocity contour of the lid driven One sided square cavity for (a) u ,Re. No.=2000, (b) v, Re. No.=2000, (c) u, Re. No.=5000, (d) v,Re. No.=5000, Grid 501×501

defined as the ratio of the height to the width. After validating the code of one-sided lid-driven cavity flow by using the finite volume SIMPLE technique, we analyzed deep lid-driven cavity fluid flow under three different aspect ratios (AR) $K = 1, 4, 6$. The two-sided lid-driven deep cavity flow for different aspect ratios, the geometry, and boundary conditions are shown in Figure 6. These two-sided lid movements produce the various vortices based on the Reynolds numbers under the different aspect ratios. They are categorized as Primary Vortex (PV_i, $i = 1$ to 6) and Secondary Vortex (BSV_i and TSV_i).

The significance of boundary conditions in any simulation process cannot be overstated. In finite volume simple algorithm technique, the simple bounce-back and no-slip boundary conditions are commonly used. In this study, the boundary conditions applied to the four sides of the cavity are illustrated in Figure 6. The performance of a two-sided deep lid-driven cavity is explored across a range of Re values from 100 to 5000 and for a variety of various aspect ratios. The findings are summarised in terms of the stream function, the midplane-u and midplane-v velocities, and the velocity contours. However, due to the primary disadvantage of using a high grid size, which is increased processing time and memory consumption, using a large grid size is not a practical option. The amount of time and space required for computing rises as the grid size grows. The optimal grid size must be determined in order to achieve acceptable

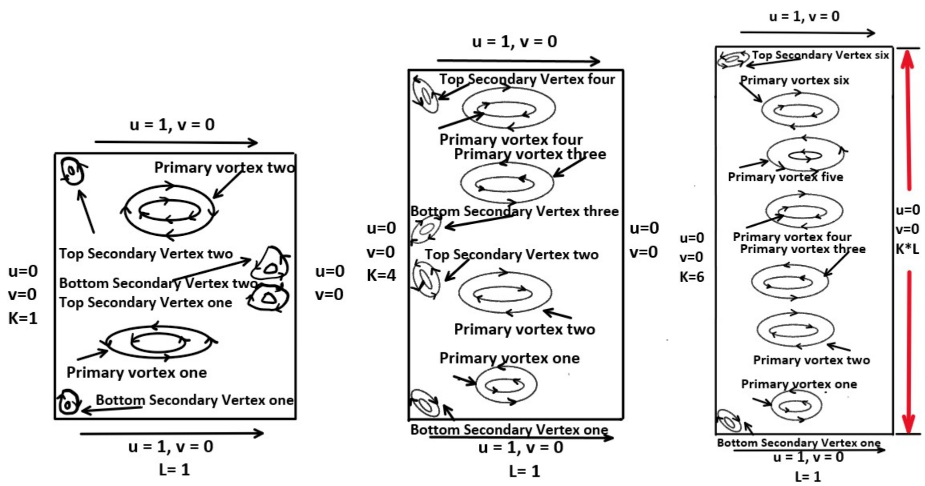

(a) (b) (c)

FIGURE 6. Geometry, Vortices and Boundary conditions of 2D lid-driven two sided deep cavity flow (a) AR K=1, (b) AR K=4, (c) AR K=6

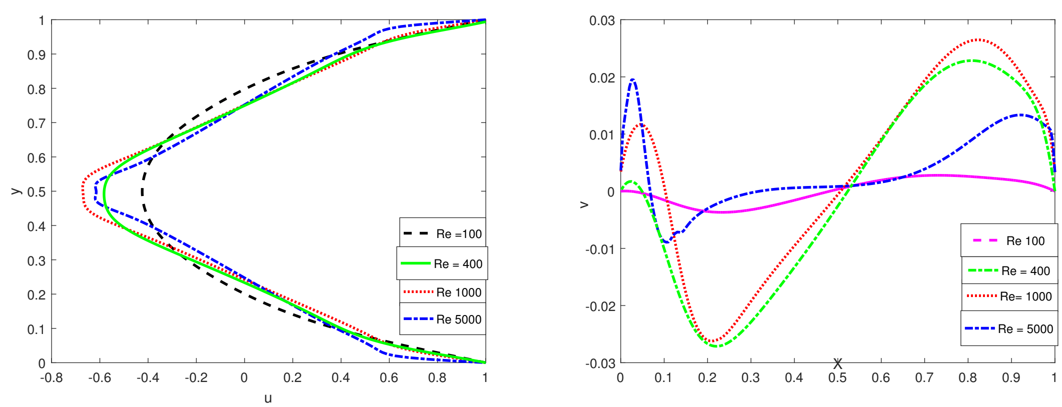

(a) (b)

FIGURE 7. (a) Centerline velocity u for aspect ratio $K = 1$ of two-sided cavity flow, (b)Centerline velocity v for aspect ratio $K = 1$ of two-sided cavity flow

accuracy in the shortest period of time. As a consequence, the current simulations are carried out for rectangular deep lid driven cavities with a range of Re and grid sizes and a range of aspect ratios, as seen in the Figure 4 to Figure 15.

Two-sided deep lid driven cavity for aspect ratio (AR) $K = 1$, Figures 4 and 7 show the centerline velocity and Figure 8 velocity contours at different Reynolds numbers (100, 400, 1000, and 5000) for gride 201. Figure 4 shows the midplane u-velocities for different Reynolds numbers. The maximum velocity in the top and bottom walls are represented as 1 since both walls move in the same direction. When Re increases, there is a linear change in the velocity profile in the middle of the cavity. Figure 7 shows the midplane v-velocities for different Reynolds numbers. The velocity in the left and right walls are represented as 0 since both walls are kept stationary.

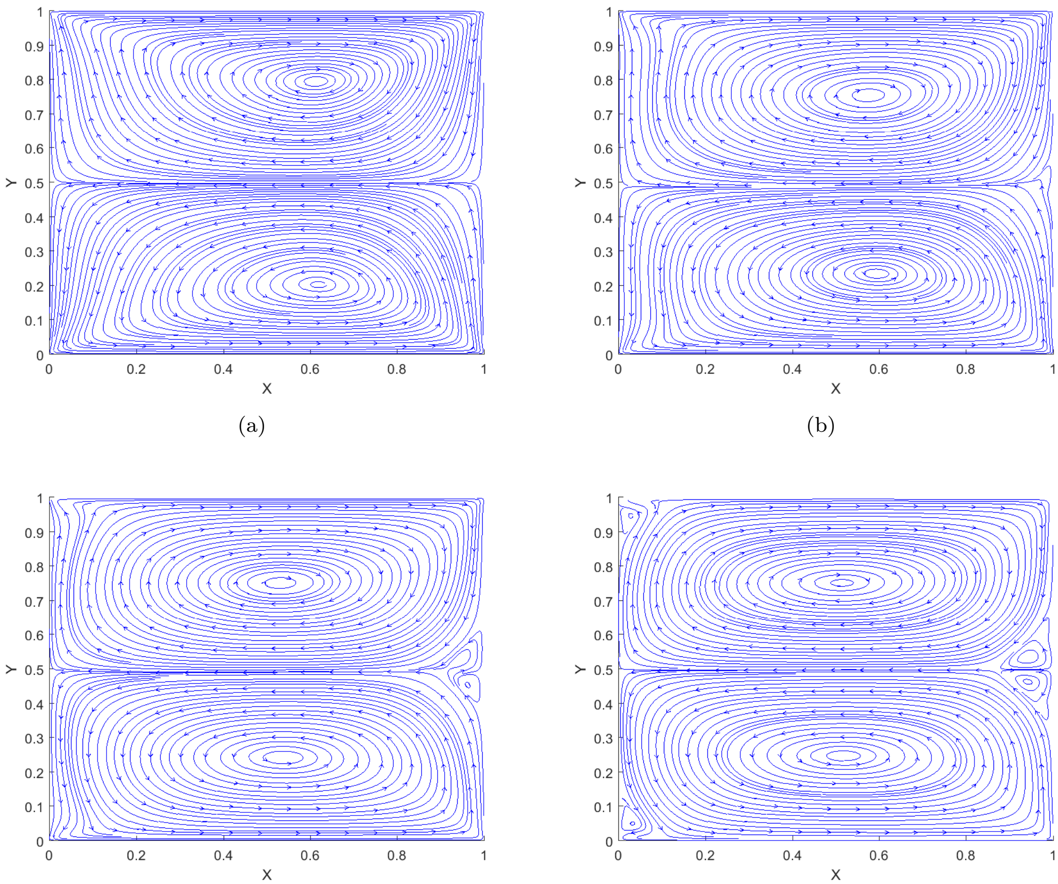

(a) (b) (c) (d)

FIGURE 8. Streamlines contour for aspect ratio $K = 1$ of two-sided cavity flow (a) Re. No.=100, (b) Re.No.=400, (c) Re.No.=1000, (d) Re.No.=5000, Grid 201×201

For K = 1, Figure 8 illustrates the streamline flow patterns in the lid-driven cavity under steady-state conditions. The findings indicate that each velocity vector contributes to the formation of an important vortex. For Reynolds number 100, two major vortexes are seen rotating in the velocity direction. They are symmetrical along the horizontal line. When Re is increased, however, a secondary vortex forms at the right boundary that pivots in the opposite direction of the applied velocity, and the flow patterns become symmetrical along the horizontal mid-plane. As the Reynolds number rises, the size of the secondary vortex steadily becomes larger. Between 1000 and 5000, however, there is little difference in the upper Re. When taking refine grid 201×201 then we get stable four main vortexes, the graph results can be found in the Supplementary Information with Figure S1 to Figure S8. It can be noticed that stream contours primary vortex (PV_1 & PV_2) arise at Re=100 as shown in Figure 8 (a). The secondary vortex (BSV_i & TSV_i, $i = 1, 2$) started to arise at Re=1000. The velocity contour of u and v for the aspect ratio of $K = 1$ of two side lid-driven cavities of the Re numbers 5000 on gride 201 as per Figure 9.

Table 4 represents the vortex position for Reynolds numbers 100, 400, 1000, and 5000. We also observed the vortex movement when we increased the Reynolds numbers shown in the Table 4. From Figure 9 and Table 4, it is clear that two primary vortexes arise. When the Reynolds number increases, then two secondary vortexes (TSV_1 & BSV_2) arise at 1000 Re number. Also, we observed that four secondary vortex (TSV_1, BSV_1, TSV_2 & BSV_2) arise at 5000 Re

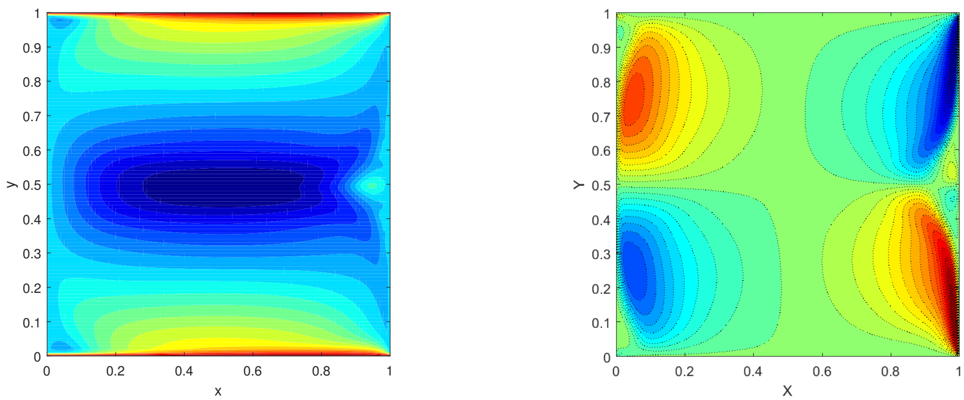

(a) (b)

FIGURE 9. Velocity contour of aspect ratio $K = 1$ for (a) u-velocity ,Re No.=5000, (b) v-velocity, Re No.=5000,on Grid 201×201

TABLE 4. Vortex profile of aspect ratio $K = 1$ of two-sided cavity flow

AR (K)	Re	Vortex position	PV_1	BSV_1	TSV_1	PV_2	BSV_2	TSV_2
K=1	100	x	0.6061	-	-	0.5944	-	-
		y	0.2096	-	-	0.8049	-	-
	400	x	0.5914	-	-	0.5769	-	-
		y	0.248	-	-	0.7729	-	-
	1000	x	0.5335	-	0.9624	0.5287	0.9445	-
		y	0.2610	-	0.4612	0.7672	0.5461	-
	5000	x	0.5195	0.03333	0.9443	0.5176	0.9483	0.02343
		y	0.2618	0.05556	0.4693	0.7617	0.5558	0.9486

number. It is obvious from Table 5 that the numerical technique takes more computational time and more iterations until it approaches the convergence criteria as Reynolds increases.

For two-sided deep lid driven cavity of aspect ratio $K = 4$, Figure 4 and 4 show the centerline velocity and Figure 11 velocity contours at different Reynolds numbers (100, 400, 1000, and 5000) for gride 201. Figure 4 shows the midplane u-velocities for different Reynolds numbers. The maximum velocity in the top and bottom walls are represented as 1 since both walls move in the same direction. When Re increases, there is a linear change in the velocity profile in the middle of the cavity. Figure 4 shows the midplane v-velocities for different Reynolds numbers. The velocity in the left and right walls are represented as 0 since both walls are kept stationary.

As demonstrated in Figure 11, the four principal vortexes are visible for the deep shallow cavity (K = 4) even at a low Reynolds number (Re = 100). However, when the Reynolds number increases, the form and intensity of those primary vortexes grow. At the preliminary phase, secondary vortex formations mix with primary vortices, resulting in the development of primary vortices. This impact is consistent with the findings of Arun et al. [5]. When taking refine grid 201×201 then we get stable four main vortexes, the graph results can be found in the Supplementary Information with Figure S9 to Figure S16. From Figure 11, it can be noticed that stream contours primary vortex ($PV_i,\ i = 1$ to 4) arise at Re=100. The secondary vortex (BSV_i & $TSV_i,\ 1 \leq i \leq 4$) start to arise at Re=5000. The velocity contour of u and v for the aspect ratio of $K = 4$ of the two-sided deep lid-driven cavity of the Re numbers 5000 on gride 201 as per Figure 12.

Table 5. Number of iterations and time(second) for convergence

AR	Renols number	Gride size	Convergence Iterations (error $= 10^{-7}$)	Time(s)
K=1	100	51*51	8764	29.9
		101*101	29176	295.96
		201*201	92837	4530.58
	400	51*51	12774	40.579
		101*101	29792	396
		201*201	96321	5248.262
	1000	51*51	13871	42.62
		101*101	36941	365.88
		201*201	107348	4216.006
	5000	51*51	42309	108.02
		101*101	56807	687.054
		201*201	186971	9956.242
K=4	100	51*51	8558	27.239
		101*101	28692	274.383
		201*201	89403	3356.672
	400	51*51	8985	30.818
		101*101	31070	298.174
		201*201	100571	3781.04
	1000	51*51	12013	34.994
		101*101	33057	311.252
		201*201	98833	3766.525
	5000	51*51	140387	330.702
		101*101	461637	4291.589
		201*201	1527990	57596.48
K=6	100	51*51	10322	32.684
		101*101	31836	298.517
		201*201	91986	3468.845
	400	51*51	10729	33.077
		101*101	36687	347.742
		201*201	112494	4220.722
	1000	51*51	12102	35.999
		101*101	36961	346.141
		201*201	116220	4354.334
	5000	51*51	111642	263.321
		101*101	391936	3709.764
		201*201	1270320	48431.15

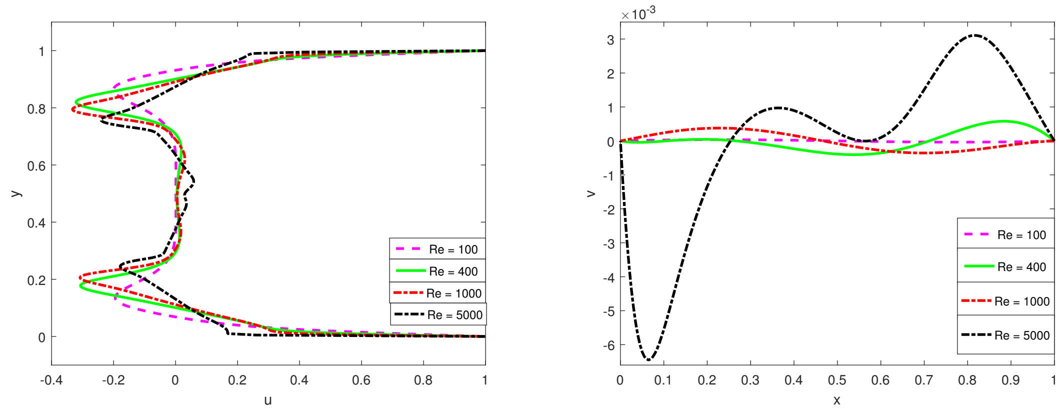

(a) (b)

FIGURE 10. (a) Centerline velocity u for aspect ratio $K = 4$ of two-sided cavity flow, (b) Centerline velocity v for aspect ratio $K = 4$ of two-sided cavity flow

TABLE 6. Vortex profile of aspect ratio $K = 4$ of two-sided cavity flow

AR (K)	Re	Vortex position	PV_1	PV_2	PV_3	PV_4	BSV_1	TSV_2	BSV_3	TSV_4
K=4	100	x	0.5928	0.5245	0.5399	0.5778	-	-	-	-
		y	0.328	1.475	2.601	3.646	-	-	-	-
	400	x	0.5556	0.4226	0.4415	0.5559	-	-	-	-
		y	0.381	1.203	2.897	3.641	-	-	-	-
	1000	x	0.5429	0.3331	0.378	0.5311	-	-	-	-
		y	0.5013	1.218	2.827	3.623	-	-	-	-
	5000	x	0.5254	0.4674	0.4679	0.5203	0.06657	0.09012	0.1237	0.06533
		y	0.5841	1.558	2.562	3.55	0.1746	1.921	2.095	3.844

Table 6 represents the vortex position for Reynolds numbers 100, 400, 1000, and 5000. We also observed the vortex movement when we increased the Reynolds numbers shown in the Table 6. From Figure 12 and Table 6, it is clear that four primary vortexes arise. When Reynolds number increases, then four secondary vortex (BSV_1, TSV_2, BSV_3, & TSV_4) arise at 5000 Re number. It is obvious from Table 5 that the numerical technique takes more computational time and more iterations until it approaches the convergence criteria as Reynolds increases.

For two sided deep lid driven cavity of aspect ratio $K = 6$, Figure 4 and 13 show the centerline velocity and Figure 14 velocity contours at different Reynolds numbers (100, 400, 1000, and 5000) for gride 201. It is noticed that the centreline velocity (u) profile reaches the upper right and lower right corners of the cavity when Re numbers increases. As demonstrated in Figure 14, the six principal vortexes are visible for the deep lid driven cavity (K = 6) even at a low Reynolds number (Re = 100). However, taking 51×51 grid for Reynolds numbers 100, 400, 1000, & 5000 then we get five main vortexes. When taking refine grid 201×201 then we get stable six main vortexes, the graph results can be found in the Supplementary Information with Figure S17 to Figure S22. From Figure 14, it can be noticed that stream contours primary vortex (PV_i, $i = 1$ to 6) arise at Re=100. The secondary vortex (BSV_i & TSV_i, $1 \le i \le 6$) start to arise at Re=5000. The velocity contour of u and v for the aspect ratio of $K = 6$ of two-sided deep lid-driven cavity of the Re number 5000 on gride 201 as per Figure 15.

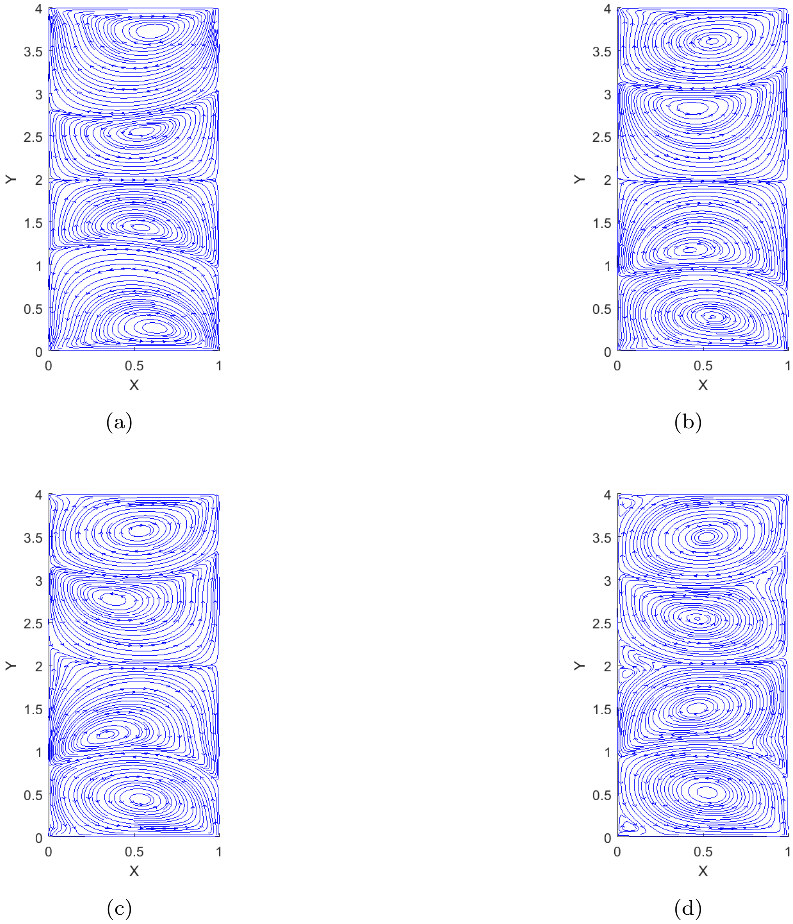

FIGURE 11. Streamlines contour for aspect ratio $K = 4$ of (a) Re. No.=100, (b) Re.No.=1000, (c) Re.No.=5000, Grid 201×201

Table 7 represents the vortex position for Reynolds numbers 100, 400, 1000, and 5000. We also observed the vortex movement when we increased the Reynolds numbers shown in the Table 7. From Figure 15 and Table 7, it is clear that six primary vortexes arise. When the Reynolds number increases, then two secondary vortexes (BSV_1, & TSV_6) arise at 5000 Re number. It is obvious from Table 5 that the numerical technique takes more computational time and more iterations until it approaches the convergence criteria as Reynolds increases.

5. Conclusion

The evidence from this study points towards the idea that the two sided deep lid-driven cavity under different aspect ratios ($K = 1,\ 4$ & 6) has not been studied except that it has academic value in the study of the dynamics of vortices at corners, which depend on Reynolds numbers & walls in the direction of movement. First, to validate the numerical solution, lid-driven one-sided square cavities have been studied, and the results are validated by related results in the literature, where they are shown with the complete agreement between the data values. Second, in different uninvestigated cases of the two-sided deep lid-driven cavities, we have obtained satisfactory results after investigating under different aspect ratios. However, for situations when there is only one side and two sides, such as a square and a rectangle, a simplified centerline velocity profile and velocity contour plots are used. In addition, for

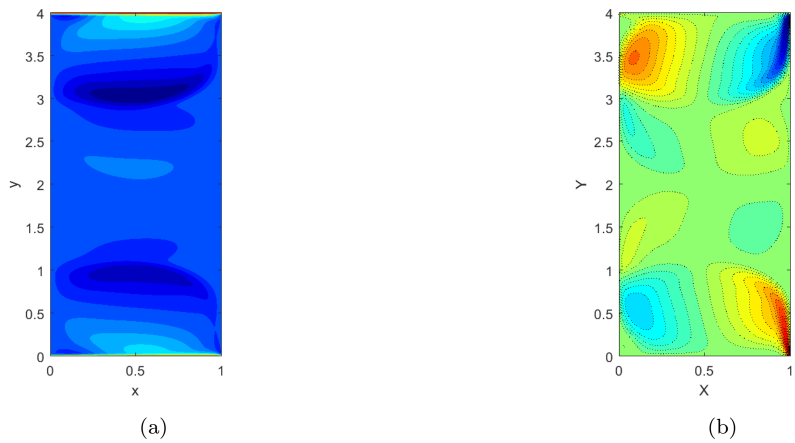

FIGURE 12. Velocity contour of aspect ratio $K = 4$ for (a) u-velocity ,Re No.=5000, (b) v-velocity, Re No.=5000,on Grid 201×201

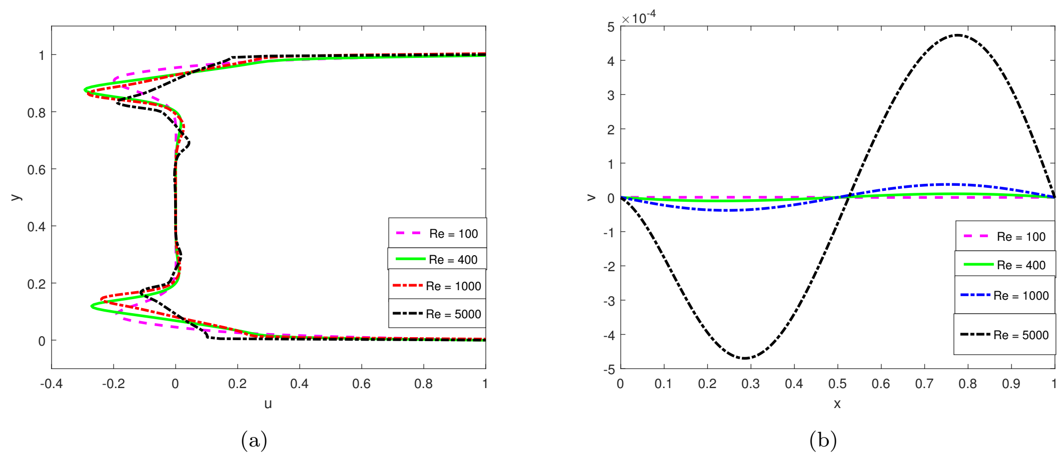

FIGURE 13. (a) Centerline velocity u for aspect ratio $K = 6$ of two-sided cavity flow, (b) Centerline velocity v for aspect ratio $K = 6$ of two-sided cavity flow

TABLE 7. Vortex profile of aspect ratio $K = 6$ of two-sided cavity flow

AR (K)	Re	Vortex position	PV1	PV2	PV3	PV4	PV5	PV6	BSV1	TSV6
K=6	100	x	0.5628	0.4644	0.4889	0.4615	0.4654	0.5462	-	-
		y	0.5482	1.4490	2.7030	3.4490	4.7030	5.5730	-	-
	400	x	0.5623	0.4477	0.4893	0.4869	0.4606	0.5550	-	-
		y	0.4716	1.301	2.603	3.496	4.722	5.499	-	-
	1000	x	0.5469	0.3733	0.4794	0.4566	0.3956	0.5321	-	-
		y	0.5024	1.329	2.530	3.703	4.694	5.488	-	-
	5000	x	0.544	0.4156	0.3666	0.6001	0.4565	0.5246	0.5879	0.05869
		y	0.6182	1.535	2.361	3.804	4.571	5.561	0.1716	5.817

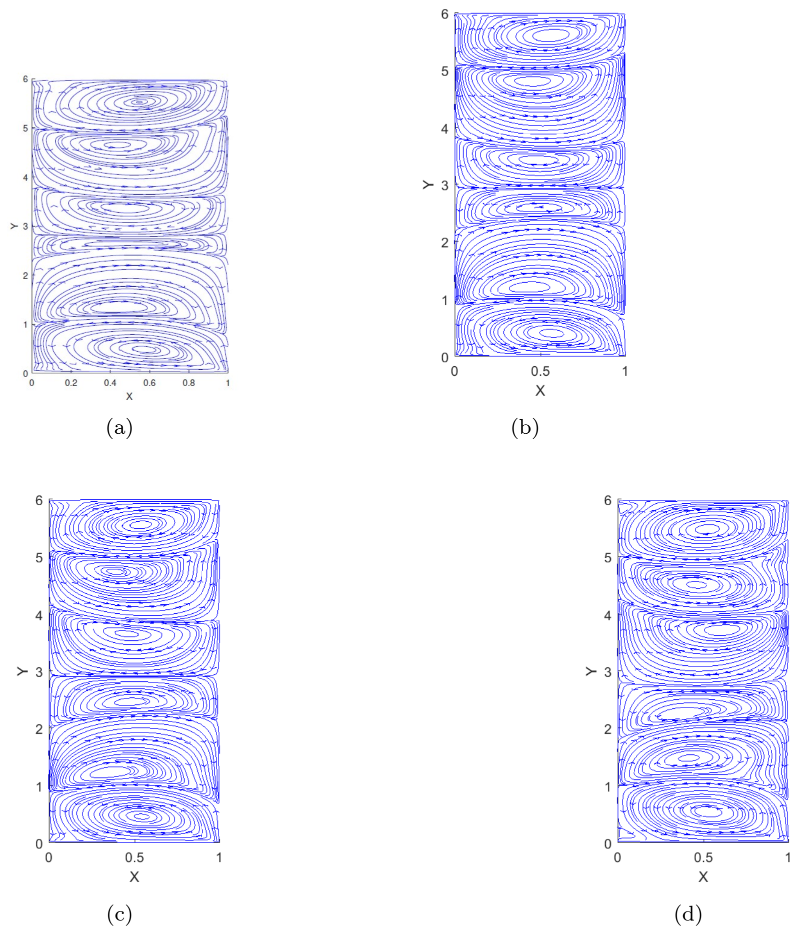

FIGURE 14. Streamlines contour for aspect ratio $K = 6$ of (a) Re. No.=100, (b) Re.No.=1000, (c) Re.No.=5000, Grid 201×201

each Reynolds number, the locations of the main and secondary vortices in the square and rectangular deep lid cavities are distinct. As the Re number rises, the primary vortex (PV) approaches the cavity centre and the secondary vortex (SV) increases in size and intensity. While studying flow properties such as Reynolds number and aspect ratio, various Reynolds numbers (100, 400, 1000, and 5000) and aspect ratios (1, 4, and 6) are utilised in the present research. These results are very robust. As we discussed in the previous section, different streamline patterns, velocity profiles, and velocity contours are all detailed in great detail in order to make sense of them. Different streamline patterns are produced when Re and aspect ratio K are changed. The velocity profiles in the cavity are shown by the graphs of u and v velocity. To demonstrate this, the experiment shows that $K = 4$ yields no secondary vortex, but three secondary vortexes are produced for walls travelling in the same direction when Re is increased to 5000. However, only two secondary vortexes are produced for $K = 6$ even when Re is increased. The graphs of u and v velocity describe the velocity profile formed in the cavity. The results provide an important source for researchers to validate their results. The problems are either external or internal flows, such as flow in a channel or flow over a simply shaped obstacle. Future work will explore the changes in the aspect ratio of heat transfer on non-Newtonian fluid flow.

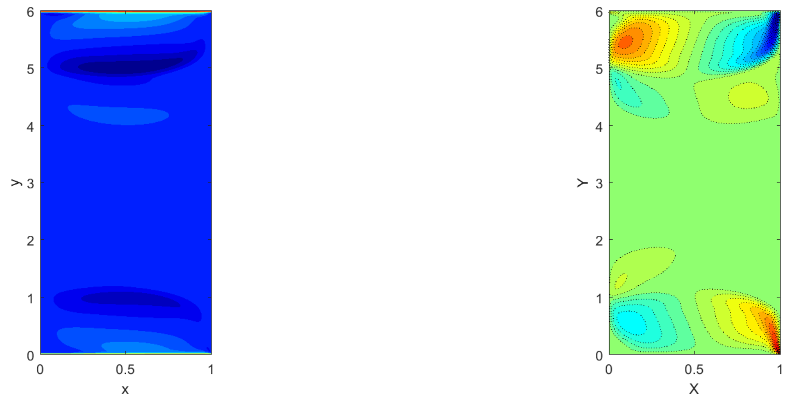

(a) (b)

FIGURE 15. Velocity contour of aspect ratio $K = 6$ for (a) u-velocity ,Re No.=5000, (b) v-velocity, Re No.=5000,on Grid 201×201

6. Acknowledgments

The authors would like to express our special thanks and gratitude to DST, Gujcost, and C-DAC high-performance computing clusters, PARAM Shavak of KSV.

Nomenclatures

u	x-axis velocity component(m/s)
u^*	x-axis approximate velocity (m/s)
u'	x-axis correction velocity (m/s)
v	y-axis velocity component(m/s)
v^*	y-axis approximate velocity(m/s)
v'	y-axis correction velocity (m/s)
p	pressure(N/m^2)
p^*	guessed pressure(N/m^2)
p'	correction pressure(N/m^2)
i	x-direction node location
j	y-direction node location
Δx	x-direction spatial step
Δy	y-direction spatial step

Abbreviations

$2D$	two dimensional
Re	Reynolds number
AR	aspect ratio
K	aspect ratio
SIMPLE	semi implicit method for pressure linked equation
HPC	high performance computing
FVM	Finite volume technique
PV	primary vortex
Right-SV	right secondary vortex
Left-SV	left secondary vortex
Left-USV	left upper secondary vortex
PV_i	i^{th} primary vortex
BSV_i	i^{th} bottom secondary vortex
TSV_i	i^{th} top secondary vortex

References

[1] J. D. Anderson and J. Wendt, *Computational fluid dynamics*, Springer, 1995.

[2] E. F. Anley and Z. Zheng, *Finite Difference Approximation Method for a Space Fractional Convection–Diffusion Equation with Variable Coefficients*, Symmetry, *12* (2020), 485.

[3] A. R. Appadu, J. K. Djoko, and H. Gidey, *A computational study of three numerical methods for some advection-diffusion problems*, Applied Mathematics and Computation, *272* (2016), 629–647.

[4] E. F. Anley, *Numerical solutions of elliptic partial differential equations by using finite volume method*, Pure and Applied Mathematics Journal, *5* (2015), 120–129.

[5] S. Arun and A. Satheesh, *Analysis of flow behaviour in a two sided lid driven cavity using lattice boltzmann technique*, Alexandria Engineering Journal, *54* (2015), 795–806.

[6] V. Aswin, A. Awasthi, and C. Anu, *A comparative study of numerical schemes for convection-diffusion equation*, Procedia Engineering, *127* (2015), 621–627.

[7] P. Ding, *Solution of lid-driven cavity problems with an improved SIMPLE algorithm at high Reynolds numbers*, International Journal of Heat and Mass Transfer, *115* (2017), 942–954.

[8] I. Demirdžić, Lilek Ž, and M. Perić, *Fluid flow and heat transfer test problems for non-orthogonal grids: benchmark solutions*, International Journal for Numerical Methods in Fluids, *15* (1992), 329–354.

[9] E. Erturk, *Discussions on driven cavity flow*, International journal for numerical methods in fluids, *60* (2009), 275–294.

[10] E. Erturk, T. C, Corke, and C. Gökçöl, *Numerical solutions of 2-D steady incompressible driven cavity flow at high Reynolds numbers*, International journal for Numerical Methods in fluids, *48* (2005), 747–774.

[11] E. Erturk and C. Gökçöl, *Fourth-order compact formulation of Navier–Stokes equations and driven cavity flow at high Reynolds numbers*, International Journal for Numerical Methods in Fluids, *50* (2006), 421–436.

[12] E. Erturk and O. Gokcol, *Fine grid numerical solutions of triangular cavity flow*, The European Physical Journal-Applied Physics, *38* (2007), 97–105.

[13] J. Ferziger and M. Peric, *Computational methods for fluid dynamics: Springer Science & Business Media*, 2012.

[14] U. Ghia, K. N. Ghia, and C. Shin, *High-Re solutions for incompressible flow using the Navier-Stokes equations and a multigrid method*, Journal of computational physics, *48* (1982), 387–411.

[15] D. Gismalla, *Matlab software for iterative methods and algorithms to solve a linear system*, International Journal of Engineering and Technical Research (IJETR), (2014), 2321–0869.

[16] M. M. Gupta and J. C. Kalita *A new paradigm for solving Navier–Stokes equations: streamfunction–velocity formulation*, Journal of Computational Physics, *207* (2005), 52–68.

[17] S. Hou, Q. Zou, S. Chen, G. Doolen, and A. C. Cogley, *Simulation of cavity flow by the lattice Boltzmann method*, Journal of computational physics, *118* (1995), 329–347.

[18] J. V. Indukuri and R. Maniyeri, *Numerical simulation of oscillating lid driven square cavity*, Alexandria engineering journal, *57* (2018), 2609–2625.

[19] P. K. Kundu and I. M. Cohen, *Fluid mechanics*, 2002.

[20] A. G. Kamel, E. H. Haraz, and S. N. Hanna, *Numerical simulation of three-sided lid-driven square cavity*, Engineering Reports, *2* (2020), e12151.

[21] S. Mazumder, *Numerical methods for partial differential equations: finite difference and finite volume methods*, Academic Press,(2015).

[22] F. Moukalled, L. Mangani, and M. Darwish, *The finite volume method in computational fluid dynamics*, Springer, *113* (2016).

[23] M. N. Ozisik, *Heat transfer: a basic approach*,McGraw-Hill New York,1985.

[24] H. F. Peng, K. Yang, M. Cui, and X. W. Gao, *Radial integration boundary element method for solving two-dimensional unsteady convection–diffusion problem*, Engineering Analysis with Boundary Elements, *102* (2019), 39–50.

[25] M. R. Patel and J. U. Pandya, *Numerical study of a one and two-dimensional heat flow using finite volume*, Materials Today: Proceedings, *51* (2021), 48–57.

[26] M. R. Patel and J. U. Pandya, *A research study on unsteady state convection diffusion flow with adoption of the finite volume technique*, Journal of Applied Mathematics and Computational Mechanics, *20* (2021), 65–76.

[27] D. Patil, K. Lakshmisha, and B. Rogg, *Lattice Boltzmann simulation of lid-driven flow in deep cavities*, Computers & fluids, *35* (2006), 1116–1125.

[28] O. Satbhai, S. Roy, and S. Ghosh, *Direct numerical simulation of a low Prandtl number Rayleigh–Bénard convection in a square box*, Journal of Thermal Science and Engineering Applications, *11* (2019).

[29] P. Suhas, *Numerical heat transfer and fluid flow*, Hemisphere publishing corporation, Etas-Unis d'Amérique, 1980.

[30] S. Som, *Introduction to heat transfer*, PHI learning Pvt. Ltd.,2008.

[31] G. D. Smith, *Numerical solution of partial differential equations: finite difference methods*,Oxford university press, 1985.

[32] S. S. Sastry, *Introductory methods of numerical analysis*, PHI Learning Pvt. Ltd., 2012.

[33] D. A. Von Terzi, *Numerical investigation of transitional and turbulent backward-facing step flows*, PhD thesis. The University of Arizona, 2004.

[34] H. K. Versteeg and W. Malalasekera, *An introduction to computational fluid dynamics: the finite volume method*,Pearson education, 2007.

[35] M. Xu, *A modified finite volume method for convection-diffusion-reaction problems*, International Journal of Heat and Mass Transfer, *117* (2018), 658–668.

[36] A. Yaghoubi, *High Order Finite Difference Schemes for Solving Advection-Diffusion Equation*